

Electric control of optically-induced magnetization dynamics in a van der Waals ferromagnetic semiconductor

Received: 7 September 2023

Accepted: 30 January 2024

Published online: 12 February 2024

 Check for updatesFreddie Hendriks¹, Rafael R. Rojas-Lopez^{1,2}, Bert Koopmans³ & Marcos H. D. Guimarães¹✉

Electric control of magnetization dynamics in two-dimensional (2D) magnetic materials is an essential step for the development of novel spintronic nano-devices. Electrostatic gating has been shown to greatly affect the static magnetic properties of some van der Waals magnets, but the control over their magnetization dynamics is still largely unexplored. Here we show that the optically-induced magnetization dynamics in the van der Waals ferromagnet $\text{Cr}_2\text{Ge}_2\text{Te}_6$ can be effectively controlled by electrostatic gates, with a one order of magnitude change in the precession amplitude and over 10% change in the internal effective field. In contrast to the purely thermally-induced mechanisms previously reported for 2D magnets, we find that coherent opto-magnetic phenomena play a major role in the excitation of magnetization dynamics in $\text{Cr}_2\text{Ge}_2\text{Te}_6$. Our work sets the first steps towards electric control over the magnetization dynamics in 2D ferromagnetic semiconductors, demonstrating their potential for applications in ultrafast opto-magnonic devices.

Ever since the experimental confirmation of magnetism in two-dimensional (2D) van der Waals (vdW) materials^{1,2}, researchers have tried to understand their fundamentals and to utilize their unique properties for new technologies, such as novel spintronic devices for information storage and processing^{3–6}. The use of magnetization dynamics is particularly interesting since it provides an energy efficient route to transfer and process information^{7–11}. A key challenge in this field, named magnonics, is the effective control over the magnetization and its dynamics using electrostatic means, allowing for energy efficient, on-chip, reconfigurable magnonic circuit elements^{12–14}. For conventional (three-dimensional) systems this control has been shown to be very promising to reduce the energy barriers for writing magnetic bits using spin-orbit torques^{15,16}. Nonetheless, the effect is still relatively modest^{17–20}. In contrast, 2D magnetic semiconductors provide an ideal platform for electric manipulation of magnetization. Their low density of states and high surface-to-volume ratio allow for an effective control over the magnetic parameters in these systems, such as the

magnetic anisotropy and saturation magnetization^{21–25}. Additionally, 2D magnetic semiconductors offer a bridge to another exciting field: the combination of optics and magnetism. These materials have shown to possess strong light-matter interaction and high magneto-optic coefficients which strength can be further tuned by the use of vdW heterostructures^{6,26–31}. These properties make 2D magnetic semiconductors ideal for the merger of two emerging fields: magnonics and photonics.

Most works on the electric control of magnetization in vdW magnets have focused on their magnetostatic properties, such as the magnetic anisotropy, saturation magnetization and Curie temperature, in both metallic^{32–35} and semiconducting^{21–25} materials. In contrast, their magnetization dynamics have only recently started to receive more attention, and have been studied using microwave-driven magnetic resonance^{36–43}, or time-dependent magneto-optic techniques^{44–52}. The latter were used on antiferromagnetic bilayer CrI_3 to show that its magnetic resonance frequency can be electrically tuned by tens of GHz⁵³. Nonetheless, the electric control over the

¹Zernike Institute for Advanced Materials, University of Groningen, Groningen, The Netherlands. ²Departamento de Física, Universidade Federal de Minas Gerais, Belo Horizonte, Brazil. ³Department of Applied Physics, Eindhoven University of Technology, Eindhoven, The Netherlands.

✉ e-mail: m.h.guimaraes@rug.nl

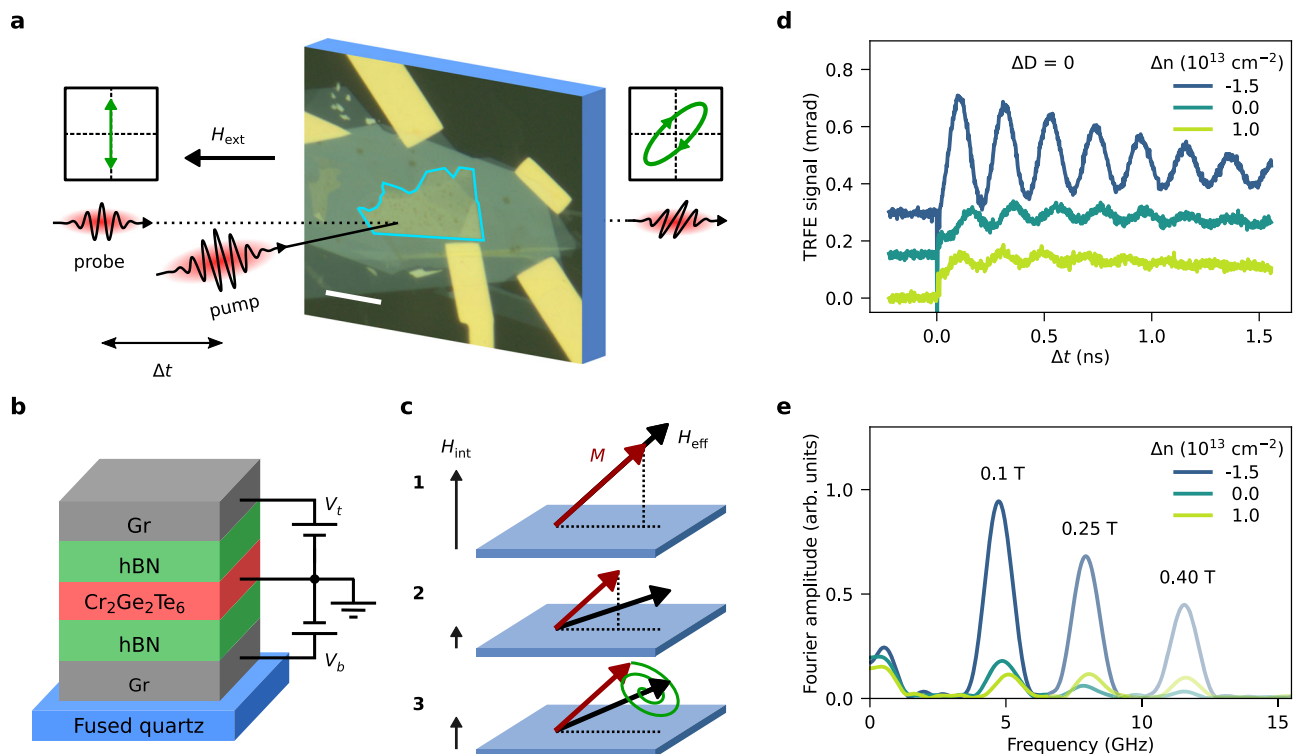


Fig. 1 | Magnetization dynamics in a CGT based heterostructure. **a** Illustration of time-resolved Faraday ellipticity measurements, combined with an optical micrograph of the sample (the scale bar is 10 μm). The CGT flake is outlined in blue. **b** Schematic of the layers comprising the sample, including electrical connections for gating. **c** Process of laser-induced magnetization precession (see main text).

d Time-resolved Faraday ellipticity traces (pump-induced change in the Faraday ellipticity) at $\mu_0 H_{\text{ext}} = 100$ mT for three different values of Δn with $\Delta D = 0$. A vertical offset was added for clarity. **e** Frequency spectrum of the oscillations in the data shown in **(d)**. Different transparencies indicate different values of H_{ext} .

optical excitation of magnetization and its subsequent dynamics in 2D ferromagnets remains to be explored.

Here we show that the magnetization dynamics of the vdW semiconductor $\text{Cr}_2\text{Ge}_2\text{Te}_6$ (CGT) can be efficiently controlled by electrostatic gating. Using ultrafast (fs) laser pulses we bring the magnetization out of equilibrium and study its dynamics with high temporal resolution through the magneto-optic Faraday effect. Using both top and bottom electrostatic gates, we independently control the gate-induced change in the charge carrier density (Δn) and the electric displacement field (ΔD) in the CGT, and show that both have drastic effects on the optically-induced oscillation amplitudes and a more modest effect on its frequency. Finally, we observe a strong asymmetric behavior on the magnetization oscillation amplitudes with respect to a reversal of the external magnetic field, which is also strongly affected by both Δn and ΔD . This asymmetry can be explained by a strong influence of coherent opto-magnetic phenomena, such as the inverse Cotton-Mouton effect and photo-induced magnetic anisotropy, on the excitation of the magnetization dynamics.

Results and discussion

Device structure and measurement techniques

Our sample consists of a 10 nm thick CGT flake, encapsulated in hexagonal boron nitride (hBN), with thin graphite layers as top gate, back gate, and contact electrodes, as depicted in Fig. 1a, b (see Methods for more details). The measurements were performed at low temperatures (10 K), with the sample mounted at 50 degrees with respect to the magnetic field axis for transmission measurements. The laser light is parallel to the magnetic field axis.

We use the time-resolved magneto-optic Faraday effect to monitor the magnetization dynamics in our system using a single-color pump-probe setup similar to the one described in refs. 54,55 (more information in Methods). The process of optical excitation of

magnetization dynamics in van der Waals magnets has been previously reported as purely thermal^{44–48,53}, similar to many studies on conventional metallic thin films^{56–58}. Here we find strong evidence that coherent opto-magnetic phenomena also play an important role in the excitation of the magnetization dynamics. The detailed microscopic description of how the magnetization dynamics is induced is described later in the article, but in short, the excitation of the magnetization dynamics can be described as follows (Fig. 1c): In equilibrium (1), the magnetization \mathbf{M} points along the total effective magnetic field \mathbf{H}_{eff} , which is the sum of the external field (\mathbf{H}_{ext}), and the internal effective field (\mathbf{H}_{int}) caused by the magnetocrystalline anisotropy (K_u) and shape anisotropy. For CGT, \mathbf{H}_{int} points out-of-plane^{2,46,59}, meaning that K_u dominates over the shape anisotropy. The linearly polarized pump pulse interacts with the sample (2), reducing the magnetization and changing the magnetocrystalline anisotropy through the mechanisms mentioned above, which causes \mathbf{M} to cant away from equilibrium. Since \mathbf{M} and \mathbf{H}_{eff} are not parallel anymore, this results in a precession of \mathbf{M} around \mathbf{H}_{eff} , while they both recover to their equilibrium value as the sample cools.

Gate control of magnetization dynamics

The dual-gate geometry of our device allows for the independent control of both the charge carrier density and the perpendicular electric field. The dependence of Δn and ΔD on the top and back gate voltages $-V_t$ and V_b , respectively—is derived in the Methods. The change in the Fermi level induced by Δn is expected to affect the magnetic anisotropy of CGT due to the different Cr *d*-orbitals composition of the electronic bands⁶⁰. The effect of ΔD is, however, more subtle. The inversion symmetry breaking caused by ΔD can allow for an energy shift of the (initially degenerate) electronic bands, potentially also modulating the magnetization parameters. Additionally, the perpendicular electric field can induce a non-uniform distribution of

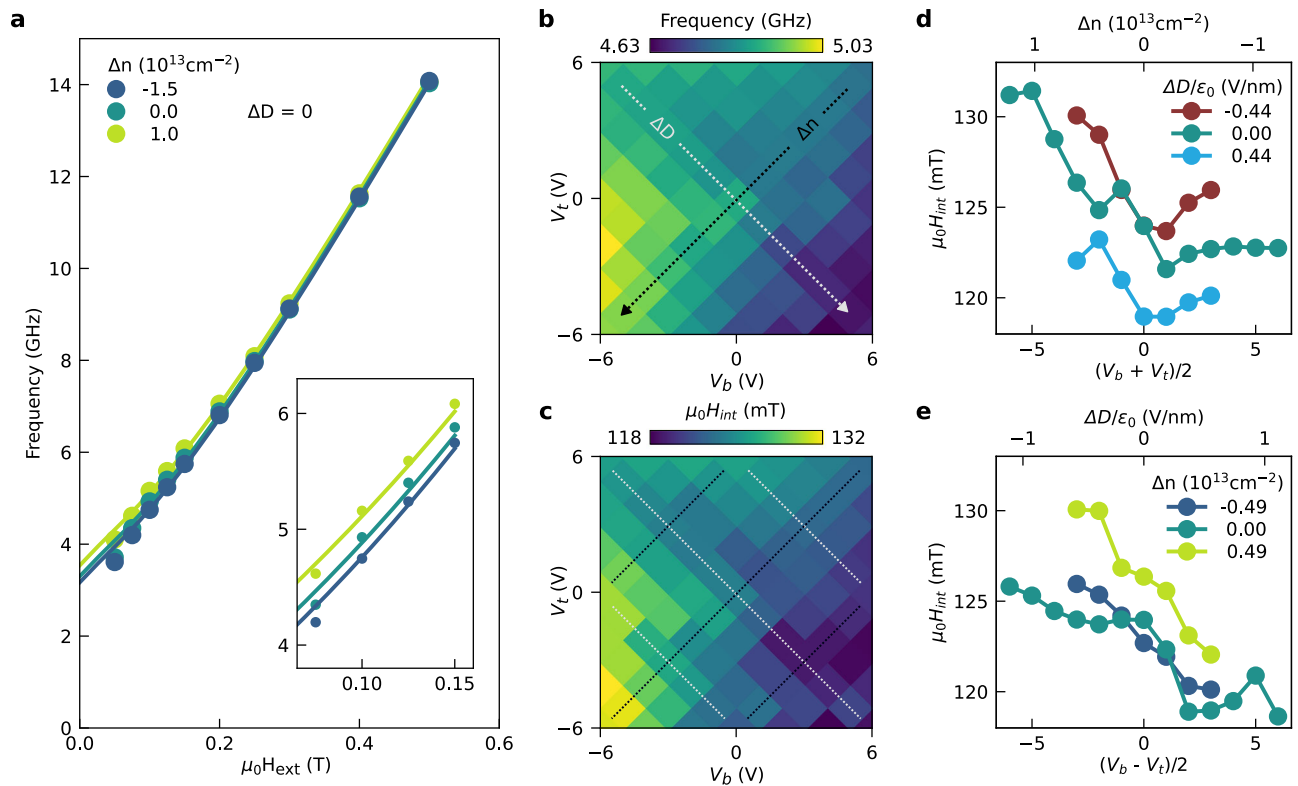


Fig. 2 | Gate-dependence of precession frequency and internal effective field. **a** Frequency of oscillations as a function of external magnetic field, for different values of Δn . The circles are the frequencies extracted from the TRFE data for $\Delta t > 26$ ps. Solid lines are best fits of Eq (1). *Inset:* Close-up of the data for low fields, showing the frequency shift due to gating. The error bars are smaller than the markers. **b** Frequency of the oscillations in the TRFE signal at $\mu_0 H_{\text{ext}} = 100$ mT for

various values of top (V_t) and back gate voltages (V_b). The black and gray arrows indicate, respectively, the directions of constant ΔD and varying Δn , and of constant Δn and varying ΔD . For other values of H_{ext} see Supplementary Fig. 10. **c** Internal effective field as a function of V_t and V_b . **d, e** The dependence of the internal effective field on Δn for fixed ΔD (**d**) and on ΔD for fixed Δn (**e**), with solid lines to guide the eye. The traces are taken along the dotted lines indicated in (**c**).

charge carriers along the thickness of the CGT flake, leading to Δn -induced local changes in the magnetization parameters.

Typical results from the time-resolved Faraday ellipticity (TRFE) measurements for different values of Δn , with $\Delta D = 0$, are shown in Fig. 1d. For $\Delta t < 0$ the signal is constant, since the magnetization is at its steady state value. All traces show a sharp increase at $\Delta t = 0$, indicating a fast laser-induced dynamics. For $\Delta t > 0$, the TRFE traces show oscillations, indicating a precession of the magnetization induced by the pump pulse.

We observe that the magnetization dynamics strongly depends on Δn , with the amplitude, frequency and starting phase of the oscillations in the TRFE signal all being affected. The most striking observation is that the amplitude of the TRFE signal increases by more than a factor of seven when Δn is changed from $1.0 \times 10^{13} \text{ cm}^{-2}$ to $-1.5 \times 10^{13} \text{ cm}^{-2}$. The observations of modulation of both the amplitude and starting phase of the oscillations hint at a change in the pump excitation process. The change in oscillation frequency due to Δn is better visible in the Fourier transform of the signals, shown in Fig. 1e (see Methods for details on the Fourier transform). This analysis clearly shows that both the frequency and amplitude of the magnetization precession are tuned by Δn . All these observations point to an effective control of the (dynamic) magnetic properties of CGT by electrostatic gating. We note that the photo-induced charge carrier density from the pump pulse is of the same order of magnitude as the gate-induced Δn . However, as discussed in Supplementary Note 7, this does not affect our conclusions about the effect of electrostatic gating.

The origin of the electric control of the magnetization dynamics can be further understood by analyzing the precession frequency at various magnetic fields and values of Δn (Fig. 2a). For magnetic fields

below 250 mT we observe a significant shift of the frequency (4–10%) by changing the charge carrier density. This is clearly visible in the inset of Fig. 2a, which shows a close-up of the data up to 150 mT. The change in precession frequency for different values of Δn strongly points towards a modulation of the magnetization parameters of CGT as a function of the Fermi level, controlled by Δn .

A quantitative analysis of the oscillation frequency (f) as a function of H_{ext} can be used to extract the magnetization dynamics parameters of the device. Our data is well described by the ferromagnetic resonance mode obtained from the Landau-Lifshitz-Gilbert (LLG) equation with negligible damping⁶¹:

$$f = \frac{g\mu_B\mu_0}{2\pi\hbar} \sqrt{|\mathbf{H}_{\text{eff}}| \left(|\mathbf{H}_{\text{eff}}| - H_{\text{int}} \sin^2(\theta_M) \right)}, \quad (1)$$

where g is the Landé g -factor, μ_B the Bohr magneton, $\mathbf{H}_{\text{eff}} = \mathbf{H}_{\text{ext}} + H_{\text{int}} \cos(\theta_M) \hat{\mathbf{z}}$, with $H_{\text{int}} = 2K_u/(\mu_0 M_s) - M_s$, M_s the saturation magnetization, and θ_M the angle between \mathbf{M} and the sample normal (z -direction). Note that in ref. 61, $|\mathbf{H}_{\text{eff}}|$ is expressed as $H_{\text{ext}} \cos(\theta_H - \theta_M) + H_{\text{int}} \cos^2(\theta_M)$ (see Supplementary Note 4). The angle θ_M is calculated by minimizing the magnetic energy in the presence of an external field, perpendicular magnetic anisotropy, and shape anisotropy⁴⁶. We obtain the g -factor and H_{ext} of the CGT by fitting the f versus H_{ext} data (e.g. the data presented in Fig. 2a) using Eq. (1), as explained in the Methods. We note that for $|\mu_0 H_{\text{ext}}| < 50$ mT, the magnetization is likely not completely saturated, since laser excitation can lead to multi-domain formation^{62,63}, which affects the magnetization dynamics. The fitting yields $g \approx 1.89$ with no clear dependence on Δn or ΔD , which is in agreement with (albeit slightly lower than) the values reported for CGT^{40,42,46} (see Supplementary Notes 5 and 6 for

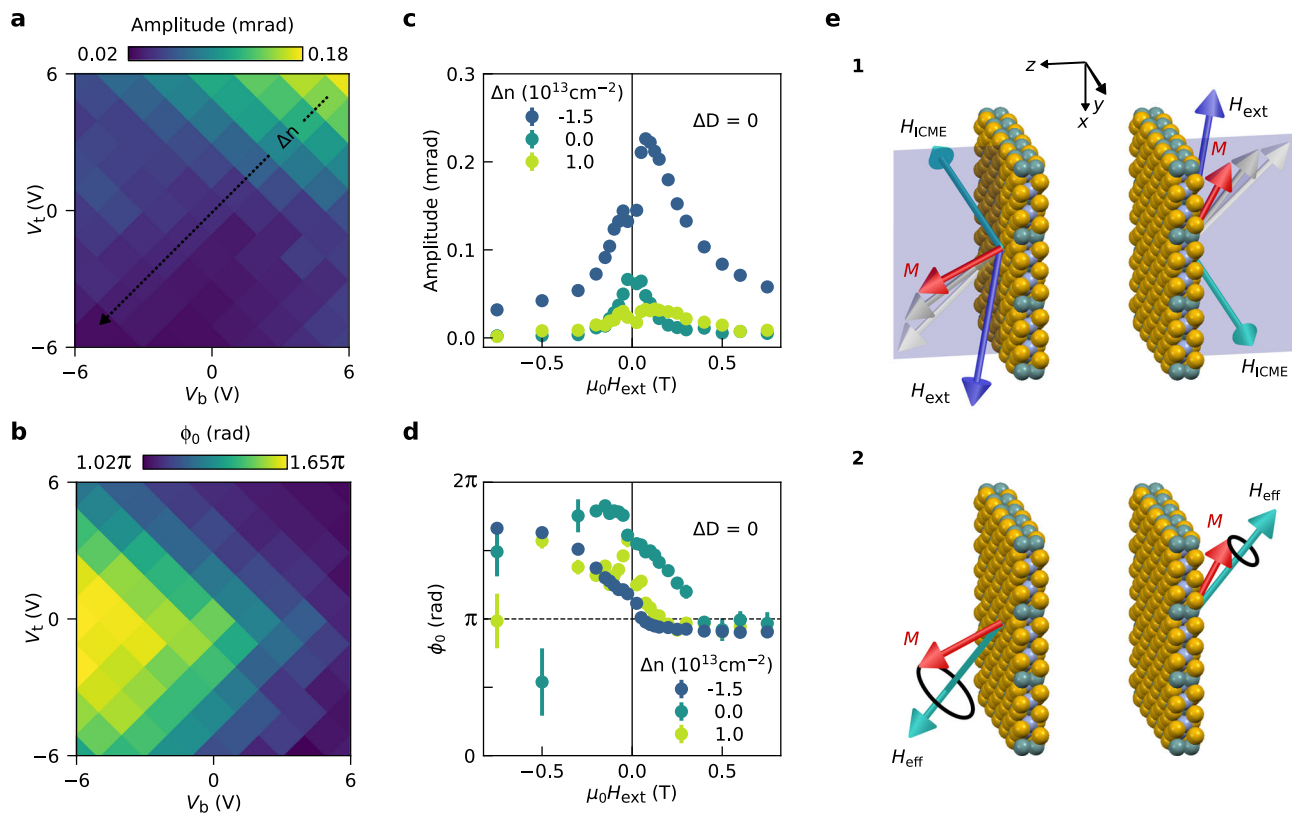


Fig. 3 | Gate dependence of magnetization precession amplitude and phase. **a, b** Gate dependence of the amplitude (**a**) and starting phase (**b**) of the oscillations in the TRFE measurements at $\mu_0 H_{\text{ext}} = 100$ mT. For other values of H_{ext} see Supplementary Figs. 8 and 9. **c, d** External magnetic field dependence of the amplitude (**c**) and starting phase (**d**) of the oscillations for different values of Δn at $\Delta D = 0$. The values are extracted from the TRFE data for $\Delta t > 26$ ps. The error bars indicate the

standard deviation obtained from the least squares fitting procedure. **e**, Schematics of the inverse Cotton-Mouton effect for opposite directions of H_{ext} . The magnetization direction is depicted by a red arrow, the external magnetic field in blue, the effective magnetic field induced by the ICME and the effective field are shown in cyan. The xz -plane is highlighted by the shaded region.

more details). We also find no clear dependence of the precession damping time (τ_{osc}) on Δn or ΔD . The intrinsic Gilbert damping we obtain from our measurements is about 6×10^{-3} (see Supplementary Note 8), in line with values found in literature^{41,46}.

The internal effective field shows a clear dependence on both V_t and V_b , as shown in Fig. 2c, with values similar to the ones found in other studies⁴⁶. Upon comparing Fig. 2c to b, one notices that the gate dependence of H_{int} is very similar to that of the precession frequency at $\mu_0 H_{\text{ext}} = 100$ mT. This suggests that the gate dependence of the precession frequency is caused by the gate-induced change in H_{int} . From the dependence of H_{int} on V_t and V_b , we extract its behavior as a function of Δn and ΔD , shown in Fig. 2d and e. We observe that H_{int} decreases with both increasing Δn and ΔD . The dependence of H_{int} on Δn is consistent with theoretical calculations⁶⁰, showing that K_u , and therefore H_{int} , is reduced upon increasing the electron density in the same order of what we achieve in our sample. The Δn dependence of H_{int} is also consistent with the dependence of the coercive field obtained from static measurements (see Supplementary Note 3), providing further evidence that the change in f is driven by a change in K_u .

Now we draw our attention to the large modulation of the oscillations in the TRFE measurements with varying gate voltage, as shown in Fig. 1d and e. Here we attribute this change in magneto-optical signal amplitude to an actual increase in amplitude of the magnetization precession (increase in the precession angle) and not to an increase in the strength of the Faraday effect. This is supported by our observation that the time-resolved measurements for different combinations of gate voltages are not simply scaled – i.e. the amplitude of the oscillations and their (ultrafast demagnetization) background scale

differently. A detailed discussion can be found in Supplementary Note 9.

Figure 3 a clearly shows that the magnetization precession amplitude is mostly affected by Δn , and to a much lesser extent by ΔD . The precession amplitude versus H_{ext} for various values of Δn is presented in Fig. 3c. As noted before, for $|\mu_0 H_{\text{ext}}| < 50$ mT the magnetization is likely not completely saturated, and therefore the magnetization dynamics can deviate from the general trend. We find that not only the precession amplitude for a given H_{ext} is strongly modulated by Δn , but its decaying trend with H_{ext} is also strongly affected. Additionally, we observe another interesting effect: the amplitude shows an asymmetry in the sign of the applied magnetic field, which is also dependent on Δn . This latter is unexpected, especially since the observed precession frequency is symmetric in H_{ext} (see Supplementary Note 11). A similar precession frequency for opposite magnetic fields indicates that the magnetocrystalline anisotropy and the saturation magnetization are independent of the sign of H_{ext} . Therefore, we conclude that the origin of the modulation of the precession amplitude is related to the excitation mechanism of the magnetization precession (see Supplementary Note 12 for the complete discussion).

To get further insight into the microscopic mechanisms involved in the optical excitation of magnetization dynamics, we analyze the magnetic field dependence of the starting phase (ϕ_0) of the precessions for different values of V_t and V_b (Fig. 3b). Unlike the amplitude, we find that ϕ_0 depends on both Δn and ΔD . As can be seen in Fig. 3d, the behavior of ϕ_0 with H_{ext} is also modulated by Δn . For a purely thermal excitation of the magnetization dynamics one would expect $\phi_0(-H_{\text{ext}}) = \pi + \phi_0(H_{\text{ext}})$ in our geometry. Nonetheless, we observe that

ϕ_0 for positive and negative magnetic fields differ by less than π . Moreover, Δn seems to also affect the trend on how ϕ_0 approaches the values at high magnetic fields. Combined with the observed asymmetry of the precession amplitude, our data strongly suggests that the optical excitation of the magnetization dynamics is not dominated by a thermal excitation (ΔK mechanism) as previously reported for other van der Waals magnets^{44–48,53}.

Opto-magnetic effects

Coherent opto-magnetic mechanisms provide possible alternatives for the optical excitation of magnetization dynamics in CGT. Here we find that our data can be explained by two of these mechanisms that are compatible with a linearly-polarized pump pulse, the inverse Cotton-Mouton effect (ICME)^{64–66} and photo-induced magnetic anisotropy (PIMA)⁶⁷, in addition to the conventional (thermal) ΔK mechanism⁶⁸. The ICME, which could be described by impulsive stimulated Raman scattering, relies on the generation of an effective magnetic field upon interaction with linearly polarized light in a magnetized medium^{64–66,69,70}. This effective magnetic field is proportional to both the light intensity and magnetization. For pulsed laser excitation, the ICME generates a strong impulsive change in H_{ext} that results in a fast rotation of the magnetization. Therefore, this effect can cause the amplitude of the precession to be asymmetric in H_{ext} ^{66,70}.

Figure 3 e illustrates how the ICME could result in an asymmetric magnetic field dependence of the amplitude. For simplicity, we only consider the y -component of the generated effective magnetic field, since this component is responsible for the asymmetry. (1) A sample with perpendicular magnetic anisotropy is subject to an external magnetic field \mathbf{H}_{ext} ($-\mathbf{H}_{\text{ext}}$) in the xz -plane, pointing in the positive (negative) direction of both axes. In equilibrium, the magnetization points along the total effective field, as indicated by the light gray arrow. During laser pulse excitation, the ICME results in an effective magnetic field along the y -axis, rotating the magnetization either towards the z -axis or the x -axis, depending on the sign of \mathbf{H}_{ext} . Additionally, the ultrafast demagnetization process leads to a reduction of the magnetization. (2) After the laser pulse, the magnetization precesses around the total effective field that is composed of \mathbf{H}_{ext} and \mathbf{H}_{int} . Depending on the sign of \mathbf{H}_{ext} , the ICME has either rotated \mathbf{M} towards or away from \mathbf{H}_{eff} , resulting in different precession amplitudes.

The second coherent mechanism for laser-induced magnetization dynamics is PIMA, which leads to a step-like change in \mathbf{H}_{eff} due to pulsed laser excitation⁶⁶. This mechanism has been reported to arise from an optical excitation of nonequivalent lattice sites (e.g. dopants and impurities), which effectively redistributes the ions and hence changes the magnetic anisotropy^{71–73}. Unlike the ICME, the PIMA mechanism is not expected to lead to an asymmetry of the magnetization precession amplitude upon a reversal of H_{ext} , because it is present for times much longer than the period of precession and therefore acts as a constant change of the effective magnetic field^{67,72–74}.

All three discussed mechanisms for inducing magnetization precession—ICME, PIMA and the ΔK mechanism—are affected by electrostatic gating. The opto-magnetic effects can be affected through a change in e.g. the polarization-dependent refractive index and the occupation of charge states of ions and impurities. Additionally, the ΔK mechanism can be affected by the changes in charge relaxation pathways through, for example, electron–electron and electron–phonon interactions. We find that the combination of the above mechanisms can describe quantitatively the starting phase and qualitatively the amplitude of the observed magnetic field dependence shown in Fig. 3 (see Supplementary Note 13). The balance between these three mechanisms affects the magnetic field dependence of the amplitude and the starting phase, increases or decreases the asymmetry in the induced precession amplitude, and changes the steepness

of the starting phase versus magnetic field graph. Therefore, since our data shows a change in these properties, we conclude that the relative strength of the mechanisms for excitation of magnetization precession are effectively controlled by electrostatic gating.

We envision that the electric control over the optically-induced magnetization precession amplitude demonstrated here can be applied to devices which make use of spin wave interference for signal processing^{12–14}. This should lead to an efficient electric control over the mixing of spin waves, leading to an easier on-chip implementation of combined magnonic and photonic circuits. Even though the control over the precession frequency shown here is still modest ($\approx 10\%$), we believe it can be further enhanced by the use of more effective electrostatic doping, such as using high- κ dielectrics or ionic-liquid gating which is capable of achieving over one order of magnitude higher changes in carrier densities than the ones reported here^{21,24,25,32,75}. Using thinner CGT would further increase the gating efficiency since the gate-induced charges are confined to a smaller volume. We note that due to the non-monotonic behavior of the magnetic anisotropy energy with changes in charge carrier density, one might expect more drastic changes on H_{int} for larger changes in Δn . This control over the magnetic anisotropy can then be used for the electrostatic guiding and confinement of spin waves, leading to an expansion of the field of quantum magnonics. Finally, the presence of coherent optical excitation of magnetization dynamics we observed in CGT should also lead to a more energy-efficient optical control of magnetization⁷⁶. Therefore, the electric control over magnetization dynamics in CGT shown here provides the first steps towards the implementation of vdW ferromagnets in magneto-photonic devices that make use of spin waves to transport and process information.

Methods

Sample fabrication

The thin hBN and graphite flakes are exfoliated from bulk crystals (HQ graphene) on an oxidized silicon wafer (285 nm oxide thickness). The CGT flakes are exfoliated in the same way in an inert (nitrogen gas) environment glove box with less than 0.5 ppm oxygen and water to prevent degradation. The flakes are selected using optical contrast and stacked using a polycarbonate/polydimethylsiloxane stamp by a dry transfer van der Waals assembly technique⁷⁷. First, an hBN flake (21 nm thick) is picked up, followed by the CGT flake (10 nm thick). Next, a thin graphite flake is picked up to make electrical contact with a corner of the CGT, and extends beyond the picked-up hBN flake. After this, a second hBN flake (20 nm thick) is picked up and a thin graphite flake to function as the back gate electrode. This stack is then transferred to an optically transparent fused quartz substrate finally a thin graphite flake is transferred on top the stack to function as the top gate electrode. The device is then contacted by Ti/Au (5/50 nm) electrodes fabricated using conventional electron-beam lithography and thin metallic film deposition techniques.

Measurement setup

All measurements are done at 10 K under low-pressure (20 mbar) Helium gas. The sample is mounted at an angle, such that the sample normal makes an angle of 50 degrees with the external magnetic field and the laser propagation direction.

The ~ 200 fs long laser pulses are generated by a mode-locked Ti:Sapphire oscillator (Spectra-Physics MaiTai), at a repetition rate of 80 MHz. After a power dump, the pulses are split in an intense pump and a weaker probe pulse by a non-polarizing beam splitter. The pump beam goes through a mechanical delay stage, allowing us to modify the time delay between pump and probe by a change in the optical path length. To allow for a double-modulation detection^{54,55}, the pump beam goes through an optical chopper working at 2173 Hz. The polarization of the pump is set to be horizontal (p-polarized with respect to the sample), to allow us to block the pump beam through a

polarization filter at the detection stage. The initially linearly polarized probe pulse goes through a photoelastic modulator (PEM) which modulates the polarization of the light at 50 kHz. A non-polarizing beam splitter is used to merge the pump and probe beams on parallel paths, with a small separation between them. From here, they are focused onto the sample by an aspheric cold lens with a numerical aperture of 0.55. The probe spot size (Full Width at Half Maximum) is $\sim 1.8 \mu\text{m}$ and the pump spot size is $\sim 3.4 \mu\text{m}$, both elongated by a factor of $1/\sin(50^\circ)$ because the laser hits the sample at 50° with respect to the sample normal. The fluence of the pump and probe pulses are $F_{\text{pump}} = 25 \mu\text{J}/\text{cm}^2$ and $F_{\text{probe}} = 5.7 \mu\text{J}/\text{cm}^2$, respectively. The transmitted light is collimated by an identical lens on the opposite side of the sample and leaves the cryostat. The pump beam is blocked and the probe beam is sent to a detection stage consisting of a quarter wave plate, a polarization filter, and an amplified photodetector. The quarter wave plate and the polarization filter are adjusted until they compensate for the change in polarization caused by the optical components between the PEM and the detection stage, ensuring that our signals are purely due to the rotation or ellipticity of the probe polarization induced by our samples. The first and second harmonic of the signal (50 or 100 kHz) obtained at the photodetector, which can be measured using lock-in amplifiers, are then proportional to the change in ellipticity and rotation respectively due to the Faraday effect of the sample. For the time-resolved Faraday ellipticity measurements, we use one lock-in amplifier to measure the signal corresponding to the first harmonic of the PEM at the photodetector output, and send the output of this lock-in amplifier to the input of the next lock-in amplifier, which is referenced to the frequency of the chopper. The output of the second lock-in amplifier is the pump-induced change in the Faraday ellipticity, which we call the TRFE signal for short. The sign is chosen such that a positive TRFE signal corresponds to a decrease in magnetization. For static magneto-optic Faraday effect measurements we have blocked the pump beam before reaching the sample, and we measure the first and second harmonic of the PEM in the photodetector signal simultaneously.

Calculating Δn and ΔD from the gate voltages

The gate-induced change in charge carrier density (Δn) and displacement field (ΔD) at the CGT are calculated from the applied gate voltages using a parallel plate capacitor model. The displacement field generated by the top (D_t) and back (D_b) gates is given by $D_i = \epsilon_{\text{hBN}} E_i = \frac{1}{2} \sigma_{\text{free},i}$, where i denotes t or b , $\epsilon_{\text{hBN}} = 3\epsilon_0$ is the hBN dielectric constant^{78,79} with ϵ_0 the vacuum permittivity, and σ_{free} the free charge per unit area. The applied top and back gate voltages are related to σ_{free} by $V_i = -\int D_i/\epsilon dz$. This equation, combined with the condition of charge neutrality, gives the following three relations:

$$\begin{aligned} V_t/d_t &= \frac{\sigma_t - \sigma_{\text{CGT}} - \sigma_b}{2\epsilon_{\text{hBN}}}, \\ V_b/d_b &= \frac{\sigma_b - \sigma_{\text{CGT}} - \sigma_t}{2\epsilon_{\text{hBN}}}, \\ 0 &= \sigma_t + \sigma_b + \sigma_{\text{CGT}}, \end{aligned}$$

where $d_{t,b}$ denotes the thickness of the top (21 nm) and bottom (20 nm) hBN flakes, and σ_i the free charge per unit area in the top gate (t), back gate (b), and the CGT flake. Solving this set of equations yields:

$$\begin{aligned} \sigma_t &= \epsilon_{\text{hBN}} V_t/d_t, \\ \sigma_b &= \epsilon_{\text{hBN}} V_b/d_b, \\ \Delta n &= \sigma_{\text{CGT}}/e = -\frac{\epsilon_{\text{hBN}}}{e} \left(\frac{V_t}{d_t} + \frac{V_b}{d_b} \right), \end{aligned}$$

where e is the positive elementary charge. Note that for positive gate voltages, a negative charge carrier density is induced in the CGT. For the

gate-induced change in the displacement field at the CGT layer, we get:

$$\Delta D = (\sigma_b - \sigma_t)/2 = -\epsilon_{\text{hBN}}(V_t/d_t - V_b/d_b)/2$$

Filling in the values for the thickness of the hBN flakes and dielectric constant of hBN gives $\Delta D/\epsilon_0$ and Δn at the CGT:

$$\begin{aligned} \Delta n &= -(0.79V_t + 0.83V_b) \times 10^{12} V^{-1} \text{cm}^{-2} \\ \Delta D/\epsilon_0 &= -(0.071V_t - 0.075V_b) \text{nm}^{-1}. \end{aligned}$$

Filling in the maximum gate voltage we can apply to our sample, 9 V for V_{top} and V_{back} , yields $\Delta n = -1.5 \times 10^{13} \text{cm}^{-2}$. This is a typical value for a dual-gate geometry with hBN as a dielectric^{23,53}. Throughout the main text we use $\Delta D/\epsilon_0$ instead of ΔD for easier comparison of our values of the gate-induced change in the displacement field with values mentioned in other works. Note that we use the conversion factor ϵ_0 and not the permittivity of CGT. Therefore, the values for the ΔD that we report are the equivalent electric field values in vacuum, not in CGT.

Windowed Fourier transform

The frequency spectra of the TRFE oscillations shown in Fig. 1e are calculated from the TRFE measurements using a windowed Fourier transform. The type of window used for this calculation is the Hamming window, which extends from $\Delta t = 0$ up to the last data point. The Fourier amplitude spectrum ($A(f)$) of the TRFE oscillations is calculated as

$$\begin{aligned} A(f) &= \left(\sum_{\Delta t > 0} [W_{\text{Ham}}(\Delta t)y(\Delta t) \sin(2\pi f \Delta t)]^2 \right. \\ &\quad \left. + [W_{\text{Ham}}(\Delta t)y(\Delta t) \cos(2\pi f \Delta t)]^2 \right)^{1/2}, \end{aligned}$$

where W_{Ham} is the Hamming window, y the data points of the TRFE measurements, and f the frequency.

Determining the g -factor and H_{int}

The Landé g -factor and H_{int} can be extracted by fitting the magnetic field dependence of the precession frequencies with Eq. (1). The values of g and H_{int} we obtained from the fit were, in most cases, strongly correlated. Therefore, we first determined g by fitting the data for $\mu_0 H_{\text{ext}} \geq 125 \text{mT}$, since g is most sensitive to the slope at high fields. This yields $g = 1.89 \pm 0.01$. If we further allow for an additional uncertainty in the mounting angle of the sample, the g -factor can change by ~ 0.1 . Then we determine H_{int} by fitting Eq. (1) for all remaining measurements fixing $g = 1.89$. We note that the values for H_{int} do depend on the exact value of g , but the modulation due to electrostatic gating is not affected, as is shown in Supplementary Note 5.

Extracting the magnetization precession parameters

We extract the amplitude, frequency, and starting phase of the oscillations in the TRFE measurements by fitting the data for $\Delta t > 26 \text{ps}$ with the phenomenological formula^{46,61}

$$\begin{aligned} y &= y_0 + a e^{-\Delta t/\tau_{\text{osc}}} \cos(2\pi f \Delta t - \phi_0) \\ &\quad + A_1 e^{-\Delta t/\tau_1} + A_2 e^{-\Delta t/\tau_2}. \end{aligned} \quad (2)$$

This formula describes a phase-shifted sinusoid on top of a double exponential background. The background captures the demagnetization and remagnetization of the CGT, while the sinusoid describes the magnetization precession.

Data availability

The raw data generated in this study and the processed data have been deposited in the Zenodo data base under accession code <https://doi.org/10.5281/zenodo.8321758>⁸⁰.

References

- Huang, B. et al. Layer-dependent ferromagnetism in a van der Waals crystal down to the monolayer limit. *Nature* **546**, 270–273 (2017).
- Gong, C. et al. Discovery of intrinsic ferromagnetism in two-dimensional van der Waals crystals. *Nature* **546**, 265–269 (2017).
- Gong, C. & Zhang, X. Two-dimensional magnetic crystals and emergent heterostructure devices. *Science* **363**, eaav4450 (2019).
- Ningrum, V. P. et al. Recent advances in two-dimensional magnets: physics and devices towards spintronic applications. *Research* **2020** (2020).
- Huang, B. et al. Emergent phenomena and proximity effects in two-dimensional magnets and heterostructures. *Nat. Mater.* **19**, 1276–1289 (2020).
- Wang, Q. H. et al. The magnetic genome of two-dimensional van der Waals materials. *ACS Nano* **16**, 6960–7079 (2022).
- Cornelissen, L. J., Liu, J., Duine, R. A., Youssef, J. B. & van Wees, B. J. Long-distance transport of magnon spin information in a magnetic insulator at room temperature. *Nat. Phys.* **11**, 1022–1026 (2015).
- Chumak, A. V., Vasyuchka, V. I., Serga, A. A. & Hillebrands, B. Magnon spintronics. *Nat. Phys.* **11**, 453–461 (2015).
- Lebrun, R. et al. Tunable long-distance spin transport in a crystalline antiferromagnetic iron oxide. *Nature* **561**, 222–225 (2018).
- Manipatruni, S. et al. Scalable energy-efficient magnetoelectric spin-orbit logic. *Nature* **565**, 35–42 (2019).
- Puebla, J., Kim, J., Kondou, K. & Otani, Y. Spintronic devices for energy-efficient data storage and energy harvesting. *Commun. Mater.* **1**, 24 (2020).
- Wang, Q. et al. Voltage-controlled nanoscale reconfigurable magnonic crystal. *Phys. Rev. B* **95**, 134433 (2017).
- Chumak, A. V., Serga, A. A. & Hillebrands, B. Magnonic crystals for data processing. *J. Phys. D: Appl. Phys.* **50**, 244001 (2017).
- Merbouche, H. et al. Voltage-controlled reconfigurable magnonic crystal at the sub-micrometer scale. *ACS Nano* **15**, 9775–9781 (2021).
- Fan, Y. et al. Electric-field control of spin-orbit torque in a magnetically doped topological insulator. *Nat. Nanotechnol.* **11**, 352–359 (2016).
- Jiang, M., Asahara, H., Ohya, S. & Tanaka, M. Electric field control of spin-orbit torque magnetization switching in a spin-orbit ferromagnet single layer. *Adv. Sci.* **10**, 2301540 (2023).
- Weisheit, M. et al. Electric field-induced modification of magnetism in thin-film ferromagnets. *Science* **315**, 349–351 (2007).
- Endo, M., Kanai, S., Ikeda, S., Matsukura, F. & Ohno, H. Electric-field effects on thickness dependent magnetic anisotropy of sputtered MgO/Co₄₀Fe₄₀B₂₀/Ta structures. *Appl. Phys. Lett.* **96**, 212503 (2010).
- Chiba, D. et al. Electrical control of the ferromagnetic phase transition in cobalt at room temperature. *Nat. Mater.* **10**, 853–856 (2011).
- Dietl, T. & Ohno, H. Dilute ferromagnetic semiconductors: physics and spintronic structures. *Rev. Mod. Phys.* **86**, 187–251 (2014).
- Wang, Z. et al. Electric-field control of magnetism in a few-layered van der Waals ferromagnetic semiconductor. *Nat. Nanotechnol.* **13**, 554–559 (2018).
- Huang, B. et al. Electrical control of 2D magnetism in bilayer CrI₃. *Nat. Nanotechnol.* **13**, 544–548 (2018).
- Jiang, S., Li, L., Wang, Z., Mak, K. F. & Shan, J. Controlling magnetism in 2D CrI₃ by electrostatic doping. *Nat. Nanotechnol.* **13**, 549–553 (2018).
- Verzhbitskiy, I. A. et al. Controlling the magnetic anisotropy in Cr₂Ge₂Te₆ by electrostatic gating. *Nat. Electron.* **3**, 460–465 (2020).
- Zhuo, W. et al. Manipulating ferromagnetism in Few Layered Cr₂Ge₂Te₆. *Adv. Mater.* **33**, 2008586 (2021).
- Fang, Y., Wu, S., Zhu, Z.-Z. & Guo, G.-Y. Large magneto-optical effects and magnetic anisotropy energy in two-dimensional Cr₂Ge₂Te₆. *Phys. Rev. B* **98**, 125416 (2018).
- Wu, M., Li, Z., Cao, T. & Louie, S. G. Physical origin of giant excitonic and magneto-optical responses in two-dimensional ferromagnetic insulators. *Nat. Commun.* **10**, 2371 (2019).
- Kumar Gudelli, V. & Guo, G.-Y. Magnetism and magneto-optical effects in bulk and few-layer CrI₃: a theoretical GGA + U study. *N. J. Phys.* **21**, 053012 (2019).
- Molina-Sánchez, A., Catarina, G., Sangalli, D. & Fernández-Rossier, J. Magneto-optical response of chromium trihalide monolayers: chemical trends. *J. Mater. Chem. C* **8**, 8856–8863 (2020).
- Yang, X., Zhou, X., Feng, W. & Yao, Y. Strong magneto-optical effect and anomalous transport in the two-dimensional van der Waals magnets Fe_nGeTe₂ (n = 3, 4, 5). *Phys. Rev. B* **104**, 104427 (2021).
- Hendriks, F. & Guimarães, M. H. D. Enhancing magneto-optic effects in two-dimensional magnets by thin-film interference. *AIP Adv.* **11** (2021).
- Deng, Y. et al. Gate-tunable room-temperature ferromagnetism in two-dimensional Fe₃GeTe₂. *Nature* **563**, 94–99 (2018).
- Zheng, G. et al. Gate-Tuned Interlayer Coupling in van der Waals Ferromagnet Fe₃GeTe₂ Nanoflakes. *Phys. Rev. Lett.* **125**, 047202 (2020).
- Chen, G., Zhang, Y., Qi, S. & Chen, J.-H. Gate-controlled magnetic transitions in Fe₃GeTe₂ with lithium ion conducting glass substrate. *Chin. Phys. B* **30**, 097504 (2021).
- Wu, Q. et al. Giant and nonvolatile control of exchange bias in Fe₃GeTe₂/Irradiated Fe₃GeTe₂/MgO heterostructure through ultralow voltage. *Adv. Funct. Mater.* **33**, 2214007 (2023).
- Ni, L. et al. Magnetic dynamics of two-dimensional itinerant ferromagnet Fe₃GeTe₂. *Chin. Phys. B* **30**, 097501 (2021).
- Zeisner, J. et al. Electron spin resonance and ferromagnetic resonance spectroscopy in the high-field phase of the van der Waals magnet CrCl₃. *Phys. Rev. Mater.* **4**, 064406 (2020).
- MacNeill, D. et al. Gigahertz frequency antiferromagnetic resonance and strong magnon-magnon coupling in the layered crystal CrCl₃. *Phys. Rev. Lett.* **123**, 047204 (2019).
- Zeisner, J. et al. Magnetic anisotropy and spin-polarized two-dimensional electron gas in the van der Waals ferromagnet Cr₂Ge₂Te₆. *Phys. Rev. B* **99**, 165109 (2019).
- Khan, S. et al. Spin dynamics study in layered van der Waals single-crystal Cr₂Ge₂Te₆. *Phys. Rev. B* **100**, 134437 (2019).
- Zollitsch, C. W. et al. Probing spin dynamics of ultra-thin van der Waals magnets via photon-magnon coupling. *Nat. Commun.* **14**, 2619 (2023).
- Xu, H. et al. Electrical detection of spin pumping in van der Waals ferromagnetic Cr₂Ge₂Te₆ with low magnetic damping. *Nat. Commun.* **14**, 3824 (2023).
- Cho, C. W. et al. Microscopic parameters of the van der Waals CrSbR antiferromagnet from microwave absorption experiments. *Phys. Rev. B* **107**, 94403 (2023).
- Gong, Y. et al. Strong laser polarization control of coherent phonon excitation in van der Waals material Fe₃GeTe₂. *npj 2D Mater. Appl.* **6**, 9 (2022).
- Lichtenberg, T. et al. Anisotropic laser-pulse-induced magnetization dynamics in van der Waals magnet Fe₃GeTe₂. *2D Mater.* **10**, 015008 (2023).

46. Zhang, T. et al. Laser-induced magnetization dynamics in a van der Waals ferromagnetic $\text{Cr}_2\text{Ge}_2\text{Te}_6$ nanoflake. *Appl. Phys. Lett.* **116**, 223103 (2020).
47. Sun, T. et al. Ultra-long spin relaxation in two-dimensional ferromagnet $\text{Cr}_2\text{Ge}_2\text{Te}_6$ flake. *2D Mater.* **8**, 045040 (2021).
48. Sutcliffe, E. et al. Transient magneto-optical spectrum of photo-excited electrons in the van der Waals ferromagnet $\text{Cr}_2\text{Ge}_2\text{Te}_6$. *Phys. Rev. B* **107**, 174432 (2023).
49. Bae, Y. J. et al. Exciton-coupled coherent magnons in a 2D semiconductor. *Nature* **609**, 282–286 (2022).
50. Afanasiev, D. et al. Controlling the anisotropy of a van der Waals antiferromagnet with light. *Sci. Adv.* **7**, 3096 (2021).
51. Khusyainov, D. et al. Ultrafast laser-induced spin-lattice dynamics in the van der Waals antiferromagnet CoPS_3 . *APL Mater.* **11** (2023).
52. Bartram, F. M. et al. Real-time observation of magnetization and magnon dynamics in a two-dimensional topological antiferromagnet MnBi_2Te_4 . *Sci. Bull.* **68**, 2734–2742 (2023).
53. Zhang, X.-X. et al. Gate-tunable spin waves in antiferromagnetic atomic bilayers. *Nat. Mater.* **19**, 838–842 (2020).
54. Guimarães, M. H. D. & Koopmans, B. Spin accumulation and dynamics in inversion-symmetric van der Waals crystals. *Phys. Rev. Lett.* **120**, 266801 (2018).
55. Rojas-Lopez, R. R., Hendriks, F., van der Wal, C. H., Guimarães, P. S. S. & Guimarães, M. H. D. Magnetic field control of light-induced spin accumulation in monolayer MoSe_2 . *2D Mater.* **10**, 035013 (2023).
56. Koopmans, B. et al. Explaining the paradoxical diversity of ultrafast laser-induced demagnetization. *Nat. Mater.* **9**, 259–265 (2010).
57. Kim, S. K. et al. Ferrimagnetic spintronics. *Nat. Mater.* **21**, 24–34 (2022).
58. Scheid, P., Remy, Q., Lebègue, S., Malinowski, G. & Mangin, S. Light induced ultrafast magnetization dynamics in metallic compounds. *J. Magn. Magn. Mater.* **560**, 169596 (2022).
59. Carteaux, V., Brunet, D., Ouvrard, G. & Andre, G. Crystallographic, magnetic and electronic structures of a new layered ferromagnetic compound $\text{Cr}_2\text{Ge}_2\text{Te}_6$. *J. Phys.: Condens. Matter* **7**, 69–87 (1995).
60. Ren, W.-n et al. Tunable electronic structure and magnetic anisotropy in bilayer ferromagnetic semiconductor $\text{Cr}_2\text{Ge}_2\text{Te}_6$. *Sci. Rep.* **11**, 2744 (2021).
61. Mizukami, S. et al. Gilbert damping in perpendicularly magnetized Pt/Co/Pt films investigated by all-optical pump-probe technique. *Appl. Phys. Lett.* **96** (2010).
62. Lohmann, M. et al. Probing Magnetism in Insulating $\text{Cr}_2\text{Ge}_2\text{Te}_6$ by Induced Anomalous Hall Effect in Pt. *Nano Lett.* **19**, 2397–2403 (2019).
63. Khela, M. et al. Laser-induced topological spin switching in a 2D van der Waals magnet. *Nat. Commun.* **14**, 1378 (2023).
64. Pershan, P. S., van der Ziel, J. P. & Malmstrom, L. D. Theoretical discussion of the inverse faraday effect, raman scattering, and related phenomena. *Phys. Rev.* **143**, 574–583 (1966).
65. Gridnev, V. N. Phenomenological theory for coherent magnon generation through impulsive stimulated Raman scattering. *Phys. Rev. B* **77**, 094426 (2008).
66. Kalashnikova, A. M. et al. Impulsive excitation of coherent magnons and phonons by subpicosecond laser pulses in the weak ferromagnet FeBO_3 . *Phys. Rev. B* **78**, 104301 (2008).
67. Hansteen, F., Kimel, A., Kirilyuk, A. & Rasing, T. Femtosecond photomagnetic switching of spins in ferrimagnetic garnet films. *Phys. Rev. Lett.* **95**, 047402 (2005).
68. van Kampen, M. et al. All-optical probe of coherent spin waves. *Phys. Rev. Lett.* **88**, 227201 (2002).
69. Yan, Y.-X., Gamble Jr, E. B. & Nelson, K. A. Impulsive stimulated scattering: general importance in femtosecond laser pulse interactions with matter, and spectroscopic applications. *J. Chem. Phys.* **83**, 5391–5399 (1985).
70. Kirilyuk, A., Kimel, A. V. & Rasing, T. Ultrafast optical manipulation of magnetic order. *Rev. Mod. Phys.* **82**, 2731–2784 (2010).
71. Alben, R., Gyorgy, E. M., Dillon, J. F. & Remeika, J. P. Polarization-dependent photoinduced effects in silicon-doped yttrium iron garnet. *Phys. Rev. B* **5**, 2560–2577 (1972).
72. Hansteen, F., Kimel, A., Kirilyuk, A. & Rasing, T. Nonthermal ultrafast optical control of the magnetization in garnet films. *Phys. Rev. B* **73**, 014421 (2006).
73. Shen, L. Q. et al. Dominant role of inverse Cotton-Mouton effect in ultrafast stimulation of magnetization precession in undoped yttrium iron garnet films by 400-nm laser pulses. *Phys. Rev. B* **97**, 224430 (2018).
74. Yoshimine, I. et al. Phase-controllable spin wave generation in iron garnet by linearly polarized light pulses. *J. Appl. Phys.* **116**, 043907 (2014).
75. Tang, M. et al. Continuous manipulation of magnetic anisotropy in a van der Waals ferromagnet via electrical gating. *Nat. Electron.* **6**, 28–36 (2022).
76. Stupakiewicz, A., Szerenos, K., Afanasiev, D., Kirilyuk, A. & Kimel, A. V. Ultrafast nonthermal photo-magnetic recording in a transparent medium. *Nature* **542**, 71–74 (2017).
77. Zomer, P. J., Guimarães, M. H. D., Brant, J. C., Tombros, N. & van Wees, B. J. Fast pick up technique for high quality heterostructures of bilayer graphene and hexagonal boron nitride. *Appl. Phys. Lett.* **105**, 013101 (2014).
78. Yang, F. et al. Experimental determination of the energy per particle in partially filled Landau levels. *Phys. Rev. Lett.* **126**, 156802 (2021).
79. Pierret, A. et al. Dielectric permittivity, conductivity and breakdown field of hexagonal boron nitride. *Mater. Res. Express* **9**, 065901 (2022).
80. Hendriks, F., Rojas-Lopez, R.R., Koopmans, B. & Guimarães, M.H.D. dataset of ‘Electric control of optically-induced magnetization dynamics in a van der Waals ferromagnetic semiconductor’. Zenodo <https://doi.org/10.5281/zenodo.8321758> (2023).

Acknowledgements

The authors thank Bart J. van Wees for critically reading the manuscript and providing valuable feedback, and we thank J. G. Holstein, H. Adema, H. de Vries, A. Joshua and F. H. van der Velde for their technical support. This work was supported by the Dutch Research Council (NWO) through grants STU.019.014 and OCENW.XL21.XL21.058, the Zernike Institute for Advanced Materials, the research program “Materials for the Quantum Age” (QuMat, registration number 024.005.006), which is part of the Gravitation program financed by the Dutch Ministry of Education, Culture and Science of Education, Culture and Science (OCW), and the European Union (ERC, 2D-OPTOSPIN, 101076932). Views and opinions expressed are however those of the author(s) only and do not necessarily reflect those of the European Union or the European Research Council. Neither the European Union nor the granting authority can be held responsible for them. The device fabrication and nanocharacterization were performed using Zernike NanoLabNL facilities.

Author contributions

M.H.D.G. conceived and supervised the research. F.H. designed and fabricated the samples, performed the measurements, analyzed the data, and calculated the effect of coherent excitations on the magnetization precession under M.H.D.G. supervision. F.H. and R.R.R.L. built and tested the measurement setup. F.H., M.H.D.G., and B.K. discussed the data and provided the interpretation of the results. F.H. and M.H.D.G. co-wrote the manuscript with input from all authors.

Competing interests

The authors declare no competing interests.

Additional information

Supplementary information The online version contains supplementary material available at <https://doi.org/10.1038/s41467-024-45623-2>.

Correspondence and requests for materials should be addressed to Marcos H. D. Guimarães.

Peer review information *Nature Communications* thanks the anonymous reviewers for their contribution to the peer review of this work. A peer review file is available.

Reprints and permissions information is available at <http://www.nature.com/reprints>

Publisher's note Springer Nature remains neutral with regard to jurisdictional claims in published maps and institutional affiliations.

Open Access This article is licensed under a Creative Commons Attribution 4.0 International License, which permits use, sharing, adaptation, distribution and reproduction in any medium or format, as long as you give appropriate credit to the original author(s) and the source, provide a link to the Creative Commons license, and indicate if changes were made. The images or other third party material in this article are included in the article's Creative Commons license, unless indicated otherwise in a credit line to the material. If material is not included in the article's Creative Commons license and your intended use is not permitted by statutory regulation or exceeds the permitted use, you will need to obtain permission directly from the copyright holder. To view a copy of this license, visit <http://creativecommons.org/licenses/by/4.0/>.

© The Author(s) 2024